This is a peer-reviewed, accepted author manuscript of the following research article: Khatchenko, Y. E., Yakushev, M. V., Seibel, C., Bentmann, H., Orlita, M., Golyashov, V., Ponosov, Y. S., Stepina, N. P., Mudryi, A. V., Kokh, K. A., Tereshchenko, O. E., Reinert, F., Martin, R. W., & Kuznetsova, T. V. (2022). Structural, optical and electronic properties of the wide bandgap topological insulator $Bi_{1.1}Sb_{0.9}Te_2S$. *Journal of Alloys and Compounds, 890*, [161824]. https://doi.org/10.1016/j.jallcom.2021.161824

Structural, optical and electronic properties of the wide bandgap topological insulator Bi1.1Sb0.9Te2S

Yu. E. Khatchenko[a, *], M. V. Yakushev[a, b, c], C. Seibel[d], H. Bentmann[d], M. Orlita[e], V. Golyashov[f], Y. S. Ponosov[a, c], N. P. Stepina[f], A. V. Mudriy[g], K. A. Kokh[h, i, j], O. E. Tereshchenko[f, j], F. Reinert[d], R.W. Martin[k] and T. V. Kuznetsova[a, c]

[a] *M.N. Miheev Institute of Metal Physics of UB RAS, 18 S. Kovalevskaya Str., Ekaterinburg, 620108, Russia*

[b] *Institute of Solid State Chemistry of the UB RAS, Ekaterinburg, 620990, Russia*

[c] *Ural Federal University, 19 Mira Str., Ekaterinburg, 620002, Russia*

[d] *Experimentelle Physik VII and Würzburg-Dresden Cluster of Excellence ct.qmat Universität Würzburg, Am Hubland, D-97074 Würzburg, Germany, EU*

[e] *LNCMI, 25 Martyrs Ave., BP 166, 38042 Grenoble Cedex 9, France*

[f] *Rzhanov Institute of Semiconductor Physics of SB RAS, 13 Ac. Lavrentieva Ave., Novosibirsk, 630090, Russia*

[g] *Scientific-Practical Material Research Centre of NASB, 19 P. Brovki Str., Minsk, 220072, Belarus*

[h] *V.S. Sobolev Institute of Geology and Mineralogy of SB RAS, 3 Koptyuga Ave., Novosibirsk, 630090, Russia*

[i] *Kemerovo State University, 6 Krasnaya Str., Kemerovo, 650000, Russia*

[j] *Novosibirsk State University, 1 Pirogova Str., Novosibirsk, 630090, Russia*

[k] *Department of Physics, SUPA, Strathclyde University, 107 Rottenrow, Glasgow, G4 0NG, UK*

[*]Corresponding author.

E-mail address: yulya.khatchenko@mail.ru (Yu. E. Khatchenko)

Abstract

Successful applications of a topological insulator (TI) in spintronics require its bandgap to be wider then in a typical TI and the energy position of the Dirac point in the dispersion relations to be away from the valence and conduction bands. In this study we grew $Bi_{1.1}Sb_{0.9}Te_2S$ crystals and examined their elemental composition, structural, optical and electronic properties as well as the electronic band structure. The high structural quality of the grown crystals was established by X-ray diffraction and Raman spectroscopy. Angular resolved photoelectron spectroscopy demonstrated a near parabolic character of the valence and conduction bands and a direct bandgap of 0.36 eV. The dispersion relations also revealed a Dirac cone, confirming the topological insulator nature of this material, with the position of the Dirac point being 100 meV above the valence band maximum. Far infrared reflectivity spectra revealed a plasma edge and two phonon dips. Fitting these spectra with theoretical functions based on the Drude-Lorentz model allows determination of the high frequency dielectric constant (41.3), plasma frequency (936 cm^{-1}) and the frequencies of two infrared phonons (177.7 cm^{-1} and 77.4 cm^{-1}).

Keywords: topological insulator, $Bi_{1.1}Sb_{0.9}Te_2S$, electronic structure, ARPES, far infrared, optical reflectivity.

1. Introduction

A novel quantum state of matter has been discovered in a number of materials called topological insulators (TIs). The bulk regions of TIs have insulator-like properties whereas strong spin-orbit coupling produces topologically protected surface states (SSs) with a Dirac-type dispersion cone [1]. TIs have exotic electronic properties and high potential for use in low power spintronics [2] and quantum electronics [3]. Exploration of the electronic properties in TIs is at an early stage and

new experimental studies of TIs are expected to reveal novel physical effects opening new horizons for the application of these materials.

Successfully exploiting and studying the SSs independently from the contribution of the bulk states require the bandgap to be wider than in a typical TI, along with a Dirac point isolated from the bulk states, low concentrations of bulk charge carriers as well as the ability to reproducibly grow high-quality materials. The binary tetradymites such as the Bi-chalcogenides Bi_2Se_3 and Bi_2Te_3, are widely considered as model examples of TIs. However, in both these compounds the bulk exhibits a metallic behaviour due to high populations of intrinsic defects and, furthermore, their Dirac points are buried in the valence band (VB) [4, 5].

One of the strategies for shifting the Dirac point closer to the centre of the bulk bandgap is alloying Bi_2Te_3 with Bi_2Se_3 or Bi_2S_3 to produce the ternary crystals Bi_2Te_2Se [6] and Bi_2Te_2S [6, 7], respectively. Amongst these Bi_2Te_2S is especially attractive since the high electronegativity of S decreases the absolute energy of the VB maximum [8]. However, the difference in the ionic radii of S and Te produces strain [9], which makes Bi_2Te_3-Bi_2S_3 alloys rather unstable. On the other hand, another binary topological insulator, Sb_2Te_3, has some significant advantages over the Bi-based tetradymites in having its Dirac point shifted away from the bulk band edges. Therefore, a route to shifting the Dirac point is to explore be the $Bi_{2-x}Sb_xTe_{3-y}S_y$ quaternary solid solutions. The simultaneous partial substitution of Bi and Te by Sb and S, respectively, can convert *n*-type conductivity in native Bi_2Te_2 to *p*-type in $Bi_{1.1}Sb_{0.9}Te_2S$ [6] and shift the Dirac point deeper in the bandgap and away from the bulk bands [10]. Such an approach could be very promising for the development of TIs for spintronics devices.

The majority of recent studies of TIs are concerned with non-trivial properties. However, their bulk electronic properties can also be rather unusual [11, 12]. The interest in bulk properties of these materials is also driven by their high performance in thermoelectric devices [6–8]. Parameters of the electronic structure of the bulk can be found in the literature mostly for binary

TIs (like Bi_2Se_3, Bi_2Te_3 and Sb_2Te_3). However, very little has been reported for some more recently discovered derivatives from these binary compounds [6, 13].

In this paper we report on the growth of $Bi_{1.1}Sb_{0.9}Te_2S$ crystals, prove their topological insulator nature using Angular Resolved Photoelectron Spectroscopy (ARPES), examine elemental composition, structural and electronic properties using energy-dispersive X-ray (EDX) analysis, X-ray diffraction (XRD), Raman spectroscopy and far-infrared (FIR) reflectivity.

2. Experimental details

Flat samples with sizes about 3 × 3 mm^2 and a thickness of 0.5 mm were cleaved perpendicular to the *c*-axis from a crystalline ingot (a cylinder of 5 mm diameter and 7 mm long), grown by the vertical Bridgman technique. 4N and 5N purity Bi, Sb, Te and S, were used as the source materials [14] and the growth process was carried out in a sealed, carbon coated quartz ampoule.

The composition of the samples was measured by EDX analysis carried out using JEOL JCXA -733 at an electron beam current of 1 nA and an energy of 20 keV. The component inhomogeneity was examined by EDX measurements at several points across the surface of the samples.

The structure of the grown material was examined using XRD measurements of powder and crystals carried out at room temperature employing a DRON-3 Series X-ray Automatic Diffractometer with CuKα source (α1 ~ 1.54059 Å, α2 ~ 1.54439 Å) from 12° to 125° of the 2Θ angle with an increment of 0.02°.

For the transport measurements the current flowed in the plane perpendicular to the *c* axis in the transverse geometry whereas the magnetic field *B* was always applied perpendicular to the applied current.

Raman spectra were measured using a Renishaw micro-Raman spectrometer RM 1000 equipped with a thermoelectrically cooled CCD detector. All spectra were recorded in the backscattering configuration from the crystal basal plane using an objective with 50× magnification. The “parallel” polarization geometry (with the polarization of scattered light

parallel to the polarization of incident light, XX) and the "perpendicular" one (with the polarization of scattered light perpendicular to the polarization of incident light, XY) were both used. Lasers with wavelengths λ=514 nm and λ=532 nm were used for measurements at 10 and 300 K, respectively, at a spectral resolution of 2 cm^{-1}. The laser power was held below 1 mW to avoid heating of the sample. Edge filters were used with cutoff energies of 80 cm^{-1} (514 nm) and 40 cm^{-1} (532 nm) from the respective laser line.

Reflectivity measurements were carried out in the frequency range from 0 cm^{-1} to 5000 cm^{-1} at 4.2 K using a Bruker IFS 66v/S FTIR spectrometer with a globar light source and a silicon bolometer as detector at the Laboratoire National des Champs Magnétiques Intenses in Grenoble, France. Near normal incidence reflectivity measurements were carried out on a square 3 × 3 mm^2 area of the surface of a 0.5 mm thick sample.

ARPES measurements were performed along the $\overline{\Gamma} - \overline{M}$ direction of the Brillouin zone at about 60 K and pressure below 4×10^{-10} mbar using a monochromated light beam from a Gammadata VUV 5010 He lamp ($h\nu$ = 21.2 eV) and Scienta SES 200 hemispherical electron analyser at the University of Würzburg. The samples were cleaved under vacuum (below 2×10^{-9} mbar) at room temperature. Low energy electron diffraction (LEED) was used to characterize the long-range crystalline order as well as to determine high symmetry directions.

3. Results

3.1 Energy Dispersive X-ray Microanalysis

The elemental composition, taken as the average of 20 EDX measurements in 20 different points with a statistical error of 2%, resulted in the following values: 22.0±0.4 at% of Bi, 16.9±0.3 at% of Sb, 40.3±0.8 at% of Te and 20.8±0.4 at% of S suggesting the chemical formula $Bi_{1.10}Sb_{0.85}Te_{2.02}S_{1.04}$*. An excess of Bi over Sb can be presented by the element ratio [Bi]/[Sb] = 1.30±0.05, whereas the content of sulphur is, within experimental uncertainty, half of that for*

tellurium [S]/[Te] = 0.52±0.02. The elemental composition indicates a 5% deficiency of the cations [Bi + Sb] over the anions [S + Te].

3.2 X-ray diffraction

The experimentally measured powder XRD pattern for the grown $Bi_{1.1}Sb_{0.9}Te_2S$, shown by open circles, a Rietveld refinement fit, the difference between them as well as standard set of Bragg reflections corresponding to the tetradymite structure (the $R\bar{3}m$ space group symmetry) are presented in Fig. 1(a). Lattice constants ***a*** and ***b*** of 4.186 Å as well as ***c*** of 29.937 Å were determined, giving a unit cell volume of 454.39 $Å^3$. Fig.1(b) shows the experimental XRD pattern of the $Bi_{1.1}Sb_{0.9}Te_2S$ crystal measured in the flat-plane reflection geometry. Each diffraction peak is attributed to scattering from a specific set of (*0,0,l*) parallel planes of atoms in the rhombohedral structure of tetradymite in accordance with the standard diffraction data [6,15]. Fig.1(c) shows well resolved doublets for the (0,0,30) and (0,0,33) diffraction peaks due to the CuKα1 and CuKα2 lines, highlighting the high quality of the crystal.

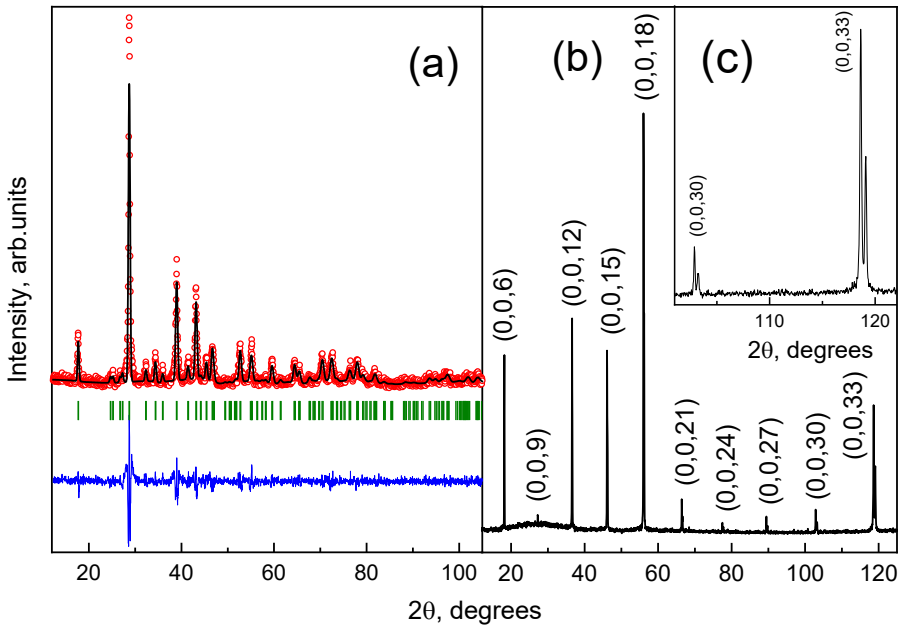

Fig. 1. (Color online). XRD patterns of $Bi_{1.1}Sb_{0.9}Te_2S$: (a) experimental data from powder (open circles), Rietveld fit (solid line) and the difference between them as well as a standard set of Bragg

reflections corresponding to the tetradymite structure; (b) experimental data from single crystal; (c) CuKα1 and CuKα2 lines for the (0,0,30) and (0,0,33) diffraction peaks for single crystal.

3.3 Transport measurements

Hall measurements at room temperature and 77 K confirmed *p*-type conductivity with hole concentrations (n_p) of $2.3 \cdot 10^{19}$ cm^{-3} and $3.5 \cdot 10^{19}$ cm^{-3}, mobilities (μ) of 190 $cm^2/(V \cdot s)$ and 350 $cm^2/(V \cdot s)$ and DC conductivities (σ) of 630 $(\Omega \cdot cm)^{-1}$ and 1700 $(\Omega \cdot cm)^{-1}$, respectively.

3.4 Raman spectroscopy

Raman spectra were measured at 10 K and 300 K for the XX and XY geometries. To determine the Raman susceptibility χ"(ω), shown in Fig. 2, the spectra were divided by the Bose factor $[1 - exp(-\hbar\omega/kT)]^{-1}$.

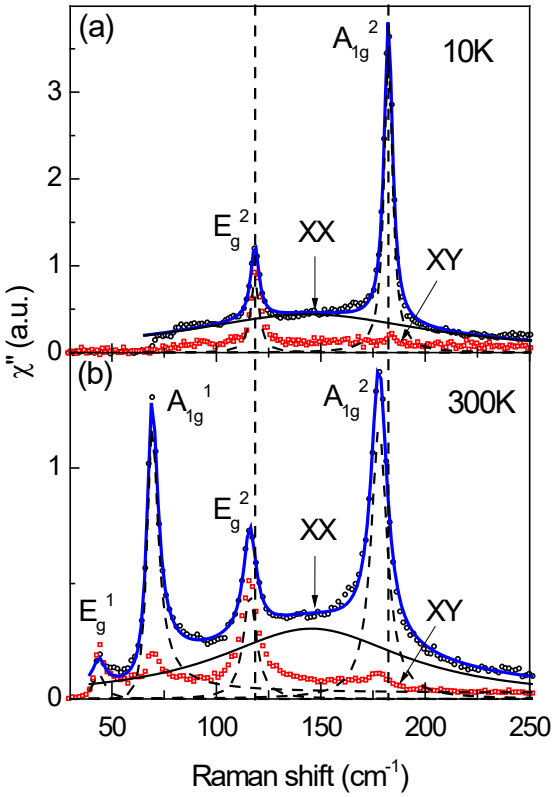

Fig. 2. The Raman susceptibility of $Bi_{1.1}Sb_{0.9}Te_2S$ obtained at two temperatures for the XX and XY geometries (points). Each spectrum was fitted with narrow peaks (dashed lines) and a broad continuum (solid lines). The vertical dashed lines show phonon positions at 10K.

The 10 K spectra in Fig.2(a) demonstrate two sharp lines at 120 cm^{-1} and 183 cm^{-1}. Increasing the temperature to 300 K, redshifts the spectral position of both lines to 116 cm^{-1} and 178 cm^{-1}, respectively. The use of the cutoff filter with a lower frequency in the 300 K measurements allowed the observation of two low-frequency phonons at 43 cm^{-1} and 69 cm^{-1} as shown in Fig.2(b). The XX geometry spectra for both 10 K and 300 K also contain a broad feature near 150 cm^{-1}.

The symmetry group analysis of $Bi_{1.1}Sb_{0.9}Te_2S$ assuming the $R\bar{3}m$ space group gives the irreducible representation:

$$\Gamma_{ph} = 2A_{1g} + 2E_g + 3A_{2u} + 3E_u, \quad (1)$$

where A_{1g} and E_g are Raman-active modes whereas the A_{1u} and E_u modes are infrared-active ones. The Raman tensors of optical phonons for the tetradymite structure allow the observation of both A_{1g} and E_g phonons in the XX geometry, while only E_g phonons can be observed in the XY geometry. The experimental Raman spectra in Fig.2 confirm this prediction: all A_{1g} and E_g peaks are seen in the XX spectra but the XY spectra contain only E_g modes at 43 and 116 cm^{-1}.

3.5 Infrared spectroscopy

A FIR reflectivity spectrum, measured at 4.2 K, is shown in Fig. 3. It reveals three prominent dips at 255 cm^{-1}, 151 cm^{-1} and 51 cm^{-1}. The experimental reflectivity spectrum was fitted with the following frequency (ω) dependent theoretical function $R(\omega)$:

$$R(\omega) = \left|\frac{\sqrt{\varepsilon(\omega)}-1}{\sqrt{\varepsilon(\omega)}+1}\right|, \quad (2)$$

where the complex dielectric function $\varepsilon(\omega)$ was calculated as a sum of Lorentz oscillators using the Drude-Lorentz model [16]:

$$\varepsilon(\omega) = \varepsilon_\infty - \frac{\omega_p^2}{\omega(\omega - i\gamma)} + \frac{S_\alpha}{\omega_\alpha^2 - \omega(\omega - i\gamma_\alpha)} + \frac{S_\beta}{\omega_\beta^2 - \omega(\omega - i\gamma_\beta)}, \qquad (3)$$

where ε_∞ is the high frequency dielectric constant, the second term is a Drude-type oscillator with damping rate γ and unscreened plasma frequency of free carriers ω_p.

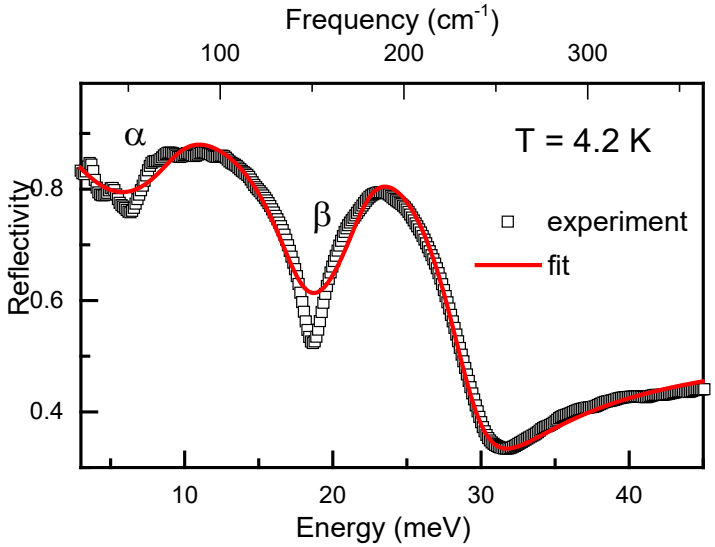

Fig. 3. An experimental FIR reflectivity spectrum at 4.2 K (symbols) and Drude-Lorentz fit (solid line).

Expression (3) also includes two more oscillators representing low frequency TO phonons with frequencies ω_α, ω_β, phonon spectral weights S_α, S_β and damping rates γ_α, γ_β for the α and β phonons, respectively. The best fit, shown in Fig.4 by solid line, allows determination of $\varepsilon_{\infty\perp}$ = 41.3 ± 0.3, parameters of the Drude oscillator ω_p = (936 ±20) cm^{-1} and γ = (114 ± 5) cm^{-1} as well as frequencies for the two phonons ω_β = (177.7 ±0.4) cm^{-1}, γ_β = (24 ± 1) cm^{-1}, S_β = (379106 ± 9590) cm^{-1} and ω_α = (77.4 ±0.7) cm^{-1}, γ_α = (26.6 ± 1.6) cm^{-1}, S_α = (661163 ± 25157) cm^{-1}.

3.6 Angle-resolved photoelectron spectroscopy

ARPES-measured energy dispersion curves of $Bi_{1.1}Sb_{0.9}Te_2S$ at 60 K are shown in Fig. 4. One can clearly see the topological surface state with its Dirac point at a binding energy of $E_B = 230$ meV, Fermi vector of (0.050 ± 0.004) 1/Å and corresponding Fermi velocity of $(6.5 \pm 1.5)\times10^5$ m/s. The VB maximum is below the Fermi level by about 0.4 eV whereas the conduction band (CB) minimum visible at 0.04 eV allows us to estimate a bulk bandgap of 0.36 eV.

The inset to Fig.4 shows the corresponding Fermi surface map revealing two characteristic spectral features. The outer ring corresponds to the Dirac state, whereas the inner circular-shaped feature represents the bulk CB.

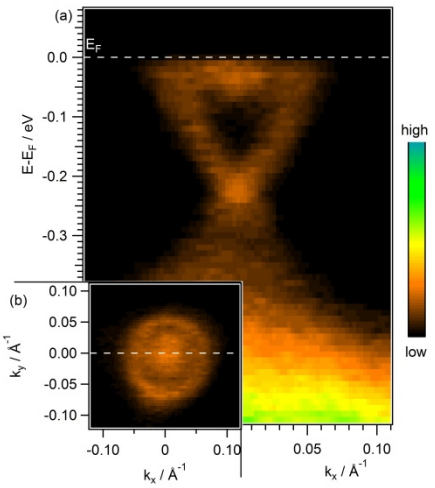

Fig. 4. ARPES energy dispersion relations of $Bi_{1.1}Sb_{0.9}Te_2S$ along the $\overline{\Gamma} - \overline{M}$ direction at 60 K. The inset displays the corresponding Fermi surface map.

4. Discussion

The chemical formula of the studied $Bi_{1.10}Sb_{0.85}Te_{2.02}S_{1.04}$ crystal is close to the $Bi_{1.1}Sb_{0.9}Te_2S$ reported in [6]. Therefore, we can expect significant similarities of the structural, optical and electronic properties of these materials. The 5% deficiency of cations in the elemental composition encourages the formation of the vacancies of Bi and Sb, V_{Bi} and V_{Sb}, interstitials of S and Te, S_i and Te_i, as well as their defect complexes such as antisite defects. Some of these defects are acceptors whereas others are donors inducing in the material a degree of compensation. The charge

carrier concentration and therefore the Fermi level position can be controlled by tuning of the cation to anion ratio.

The experimental XRD pattern for the single crystal, shown in Fig.1(b), demonstrates nearly equidistant diffraction peaks originated from the (0,0,6), (0,0,9), (0,0,12), (0,0,15), (0,0,18), (0,0,21), (0,0,24), (0,0,27), (0,0,30) and (0,0,33) crystallographic planes. The position of diffraction peaks is determined by the interplane spacing due to the Bragg's law. The main diffraction peaks in Fig.1(b) are very intensive and sharp suggesting the single crystalline nature of the sample. The experimental patterns reveal only reflections corresponding to the rhombohedral unit cell of tetradymite [6, 15]. No other peaks associated with secondary phases can be seen demonstrating a high structural quality of the crystals. Fig.1(c) shows lines due to CuKα1 and CuKα2 for the (0,0,30) and (0,0,33) diffraction peaks, which also demonstrate the homogeneity of the crystal and its well-ordered structure. The full width at half maxima (FWHM) of the (0,0,6) diffraction peak in the single crystal pattern is 0.1º for different parts of the cleaved crystals. This also strongly supports the high phase purity and structural quality of the crystal. The values determined for the ***a, b*** and ***c*** lattice constants are close to those recently reported in [6] for the related Bi-tetradymite without Sb: $Bi_2Te_{1.8}S_{1.4}$. It should be noted that in [6] these constants were determined using only XRD peak positions for 2Θ below 50° whereas our values were calculated using XRD peaks for the much wider range of 2Θ from 12° up to 105°. $Bi_{1.1}Sb_{0.9}Te_2S$ has slightly smaller lattice parameters than those in Bi_2Te_2S (***a*** = 4.32 Å, ***c*** = 30.5 Å) and Bi_2Te_3 (***a*** = 4.38 Å, ***c*** = 30.5 Å) [17] because of the smaller atomic radius of Sb with respect to that of Bi.

In order to improve the accuracy of the interpretation of the Raman spectra, the peaks in these spectra were fitted with different shapes. The best fit has been achieved using Lorentzians for all phonon lines except for the A_{1g}^1 phonon line, for which asymmetric Breit-Wigner-Fano (BWF) functions [18] were used.

Five spectral lines can be seen in the Raman spectra, which exceeds the number of vibration modes allowed by the selection rules (four). This suggests a one-mode behavior of at least three

low-frequency lines in the phonon spectra of the $Bi_{1.1}Sb_{0.9}Te_2S$ crystal lattice with a monotonic change in the phonon frequency when Bi atoms are being replaced by Sb atoms. It is surprising that the substitutional disorder, generated by such replacements, did not affect the linewidth of the high-frequency phonon A^2_{1g} at 178 cm^{-1}. Such a phonon in the binary Bi_2Te_3 at 133 cm^{-1} has a FWHM of 9 cm^{-1} [19], which is comparable with that for our quaternary crystal. However, this replacement can probably explain the twofold increase of FWHM for the low energy phonons seen in our spectra (6-8 cm^{-1} in comparison with ~3 cm^{-1} in Bi_2Te_3 [19]).

Similar to other Raman active lines, observed in our spectra, the A^2_{1g} mode is not associated with the displacement of edge atoms (which are S in our case) in the rhombohedral unit cell. For Bi_2Te_2S, the calculated frequency of the A^2_{1g} line is 157 cm^{-1}, compared to an experimental value of 148 cm^{-1}, whereas for Sb_2Te_2S the corresponding frequencies are 189 and 168 cm^{-1}, respectively [17]. Thus, the replacement of bismuth with antimony leads to a significant increase in the energy of the A^2_{1g} mode. A similar increase was also observed after bismuth in Bi_2Te_2Se was substituted with antimony to give Sb_2Te_2Se [20].

The good match of the experimental spectra, presented in Fig.2, with sums of individual Lorentzians clearly suggests the presence of a broad feature (continuum) at ~150 cm^{-1} in the XX geometry spectra. A broad continuum in the same frequency range was previously observed in the Raman spectra of $Bi_{1.5}Sb_{0.5}Te_{1.8}Se_{1.2}$ [21] and assigned to a defect mode with weak symmetry dependence. The observation of surface phonons which interact with the surface electron continuum was reported in [22] for the same frequency range of the Bi_2Se_3 Raman spectra. In our case, the continuum can be seen only in the parallel polarisation geometry and has a rather large FWHM of 100 cm^{-1} at 300 K, which is even greater at 10 K. The Raman spectrum of tin-doped $Bi_{1.1}Sb_{0.9}Te_2S$, reported in [10], is very similar to our spectra. This spectrum also shows the presence of a broad continuum in the indicated frequency range. The authors of [10] attributed the observed continuum to two-phonon scattering and a defect induced mode.

The authors of [23] also observed an additional broad line at 145 cm^{-1} in the spectrum of Bi_2Te_2Se. They attributed this line to a high concentration of the antisite defect Te-Se which induces a local mode that oscillates at its own frequency with strong damping. In our sample, antisite defects such as Te-S can also be present [24, 25]. The presence of such defects is supported by the elemental composition of our samples. An inhomogeneous distribution of such defects can lead to the observed broad continuum constituting a number of local modes with slightly different frequencies, resulting in the appearance in the Raman spectra of features, which are broader than expected for conventional phonon modes. Further detailed studies (temperature, symmetry, resonance) are needed to confidently identify the broad continuum excitations.

The energy of the high-frequency E_g and A_{1g} phonons increases with decreasing temperature whereas their width decreases, which reflects typical anharmonic effects. In general, the observed features additionally confirm the phase purity and structure of tetradymite.

A comparison of center frequencies of Raman-active phonons of TIs with the $R\bar{3}m$ space group lattice symmetry with our results is presented in Table 1. It can be seen that the simultaneous substitution of Bi and Te in Bi_2Te_3 by the lighter Sb and S, respectively, shifts all the phonon modes to higher frequencies. Notably, with respect to the parent compounds Bi_2Te_2S and Bi_2Te_3 the A_{1g} frequency increase in $Bi_{1.1}Sb_{0.9}Te_2S$ is greater than that of E_g.

Table 1. A comparison of center frequencies (cm^{-1}) of Raman and infrared-active phonons for TIs with the $R\bar{3}m$ space group lattice symmetry [17, 26].

Mode		Bi_2Te_3	Bi_2Te_2S	$Bi_{1.1}Sb_{0.9}Te_2S$
Raman	E_g^1	42.1	39.5	43
	A_{1g}^1	61.5	62	69

	E_g^2	101.5	104.5	116
	A_{1g}^2	133.5	148.5	178
Infrared	$E_u^1(\alpha)$	48		51
	$E_u^2(\beta)$	98		151

The general shape of our reflectivity spectrum, shown in Fig. 3, is very similar to those reported for Bi_2Se_3 [27, 28] where three dips were also observed although at different frequencies. Similar to the current report these features were assigned to the plasma edge minimum as well as to two phonons. The plasma frequency of ω_p = 936 cm^{-1}, determined here for $Bi_{1.1}Sb_{0.9}Te_2S$, is close to the value 832 cm^{-1} but greater than the 382 cm^{-1} reported in [29] and [28], respectively, for Bi_2Se_3.

The determined high frequency dielectric constant of $\varepsilon_{\infty\perp}$ = 41.3 for $Bi_{1.1}Sb_{0.9}Te_2S$ is close to the values of 64 and 42 from [29] for Bi_2Te_3 and Sb_2Te_3, respectively, also determined using the Drude-Lorentz model. However, a constant of ε_∞ = 9, reported in [29] for Bi_2Se_3, is significantly smaller than our value. As shown in [29] neither reflectivity spectra of Bi_2Te_3 nor of Sb_2Te_3 reveal the phonon dips observed in our spectra for $Bi_{1.1}Sb_{0.9}Te_2S$. These features in the reflectivity spectra of Bi_2Se_3 were assigned in [27] to relative transverse motion of charged Bi and Se ion modes with the E_u symmetry. Therefore, we can also assign the α and β dips in our reflectivity spectra to the $E_u^1(\alpha)$ and $E_u^2(\beta)$ infrared phonon modes shown in Table 1.

Unlike the ARPES-measured dispersion relations of $Bi_{1.1}Sb_{0.9}Te_2S$, reported in [6], Fig. 4 shows the VB and CB. Both have parabolic shapes and demonstrate the direct bandgap nature of $Bi_{1.1}Sb_{0.9}Te_2S$ and provide an opportunity to estimate a bandgap of 0.36 eV at the Γ-point of the Brillouin zone at 60 K. This bandgap is significantly wider than the 220 meV bandgap in Bi_2Se_3 [30] and 175 meV in Bi_2Te_3 [31]. The dispersion relations clearly demonstrate that the Dirac point is located at the centre of the bandgap, which is one of the necessary conditions for the application of a topological insulator. Compared with Bi_2Te_3 and Bi_2Se_3, where Dirac points are buried in the

bulk valence bands, as well as with $Bi_2Te_{1.85}S_{1.15}$ and $Bi_2Te_{1.6}S_{1.4}$, where such points are located above the VB maximum by approximately 20 and 30 meV, respectively [6, 7], the Dirac point in our $Bi_{1.1}Sb_{0.9}Te_2S$ is above the VB maximum by more than 100 meV, which makes it substantially better exposed.

The Hall measurements, dominated by the bulk properties, confirmed the *p*-type conductivity for $Bi_{1.1}Sb_{0.9}Te_2S$. However, according to the ARPES data the Fermi level at the surface has been shifted into the CB, as shown in Fig.4, suggesting *n*-type conductivity at the surface of the sample. This discrepancy can be explained by the band bending effect due to the *n*-type doping of the surface induced by the adsorption of residual gases during a lengthy experiment as reported in [32, 33].

5. Conclusions

In this study the elemental composition, structural, optical and electronic properties as well as the electronic band structure of the topological insulator $Bi_{1.1}Sb_{0.9}Te_2S$, grown by the vertical Bridgman technique, were examined. The XRD and Raman spectroscopy showed a high structural quality tetradymite lattice free from secondary phases. It had the $R\bar{3}m$ space group symmetry with lattice parameters ***a*** and ***b*** of 4.186 Å, as well as ***c*** of 29.937 Å and unit cell volume of 454.39 $Å^3$. A one-mode behaviour of the phonon spectra of $Bi_{1.1}Sb_{0.9}Te_2S$ was found with a monotonic variation of the phonon energies at the substitution as Bi atoms were substituted by Sb. A broad feature in the Raman spectra at 150 cm^{-1} suggests the presence of an antisite disorder in the sample. This is also supported by the elemental composition data. Far infrared reflectivity spectra, measured at 4.2 K, showed a plasma edge at 255 cm^{-1} and two phonon dips. Fitting the experimental reflectivity spectrum with a theoretical function based on the Drude-Lorentz model allowed determination of the high frequency dielectric constant $\varepsilon_{\infty\perp}$ = 41.3, plasma frequency 936 cm^{-1} as well as frequencies of two infrared phonons 177.7 cm^{-1} and 77.4 cm^{-1}. ARPES-measured dispersion relations revealed a near parabolic character of the valence and conduction

bands as well as a Dirac cone. The Dirac point lies well within the direct bandgap of 0.36 eV at 60 K and is positioned 100 meV above the valence band maximum, confirming the topological insulator nature of this material. We have demonstrated that the Dirac point in $Bi_{1.1}Sb_{0.9}Te_2S$ is positioned well away from the valence and conduction bands. The Fermi level can be tuned from a near bandgap centre position to the conduction band one by varying the cation to anion ratio from the ideal stoichiometry to an excess of anions.

Acknowledgments

The reported study was funded by RFBR, project number 19-29-12061. The part of optical research was carried out within the state assignment of Ministry of Science and Higher Education of the Russian Federation (theme «Spin» No AAAA-A18-118020290104-2 and No AAAA-A19-119081990020-8 and theme «Electron» No AAAAA18-118020190098-5). The study was also supported by the Russian Science Foundation (Project No.17-12-01047) in the part of the crystal growth and state assignment of ISP SB RAS (0306-2019-0007) and IGM SB RAS. The Raman measurements were partially supported by the grant of the Russian Foundation for Basic Research (Project No. 19-52-18008). This work is funded by the Deutsche Forschungsgemeinschaft (DFG, German Research Foundation) through project-ID 258499086 - SFB 1170 (A01), the Würzburg-Dresden Cluster of Excellence on Complexity and Topology in Quantum Matter–ct.qmat Project-ID 390858490 - EXC 2147.

References

[1] M.Z. Hasan and C. L. Kane, Colloquium: Topological insulators, Rev. Mod. Phys. 82 (2010) 3045-3067, https://doi.org/10.1103/RevModPhys.82.3045.

[2] L. Fu and C. L. Kane, Superconducting Proximity Effect and Majorana Fermions at the Surface of a Topological Insulator, Phys. Rev. Lett. 100 (2008), https://doi.org/10.1103/PhysRevLett.100.096407.

[3] J. E. Moore, The birth of topological insulators, Nature 464 (2010) 194-198, https://doi.org/10.1038/nature08916.

[4] K. Kuroda, M. Arita, K. Miyamoto, M. Ye, J. Jiang, A. Kimura, E. E. Krasovskii, E. V. Chulkov, H. I. and T. Okuda, K. Shimada, Y. Ueda, H. Namatame, and M. Taniguchi, Hexagonally Deformed Fermi Surface of the 3D Topological Insulator Bi_2Se_3, Phys. Rev. Lett. 105 (2010), https://doi.org/10.1103/PhysRevLett.105.076802.

[5] D.-X. Qu, S. Hor, J. Xiong, R. J. Cava, and N. P. Ong, Quantum Oscillations and Hall Anomaly of Surface States in the Topological Insulator Bi_2Te_3, Science, 329 (2010) 821-824, https://doi.org/10.1126/science.1189792.

[6] H. Ji, J. M. Allred, M. K. Fuccillo, M. E. Charles, M. Neupane, L. A. Wray, M. Z. Hasan, and R. J. Cava, $Bi_2Te_{1.6}S_{1.4}$: A topological insulator in the tetradymite family, Phys. Rev. B, 85 (2012) (R), https://doi.org/10.1103/PhysRevB.85.201103.

[7] E. Annese, T. Okuda, E.F. Schwier, H. Iwasawa, K. Shimada, M. Natamane, M. Taniguchi, I.P. Rusinov, S.V. Eremeev, K.A. Kokh, V.A. Golyashov, O.E. Tereshchenko, E.V. Chulkov, A. Kimura, Electronic and spin structure of the wide-band-gap topological insulator: Nearly stoichiometric Bi_2Te_2S, Phys. Rev. B 97 (2018), https://doi.org/10.1103/PhysRevB.97.205113.

[8] R. J. Cava, H. Ji, M. K. Fuccillo, Q. D. Gibson and Y. S. Hor, Crystal structure and chemistry of topological insulators, J. Mater. Chem. C 1 (2013) 3176-3189, https://doi.org/10.1039/C3TC30186A.

[9] L. Pauling, The formula, structure, and chemical bonding of tetradymite, $Bi_{14}Te_{13}S_8$, and the phase $Bi_{14}Te_{15}S_6$, Am. Mineral., 60 (1975) 994-997, http://www.minsocam.org/ammin/AM60/AM60_994.pdf.

[10] S.K. Kushwaha, I. Pletikosic´, T. Liang, A. Gyenis, S.H. Lapidus, Yao Tian, He Zhao, K.S. Burch, Jingjing Lin, Wudi Wang, Huiwen Ji, A.V. Fedorov, Ali Yazdani, N.P. Ong, T. Valla & R.J. Cava, Sn-doped Bi1.1Sb0.9Te2S bulk crystal topological insulator with excellent properties, Nat. Commun., 7 (2016) 11456, https://doi.org/10.1038/ncomms11456.

[11] M. Orlita, B. A. Piot, G. Martinez, N. K. Sampath Kumar, C. Faugeras, M. Potemski, C. Michel, E. M. Hankiewicz, T. Brauner, Č. Drašar, S. Schreyeck, S. Grauer, K. Brunner, C. Gould, C. Brüne & L. W. Molenkamp. Magneto-optics of massive dirac fermions in bulk Bi_2Se_3, Phys. Rev. Lett. 114 (2015), https://doi.org/10.1103/PhysRevLett.114.186401.

[12] L. Ohnoutek, M. Hakl, M. Veis, B. A. Piot, C. Faugeras, G. Martinez, M. V. Yakushev, C. Drasar, A. Materna, G. Strzelecka, A. Hruban, M. Potemski, and M. Orlita, Interband Faraday rotation in 3D topological insulator Bi_2Se_3, Sci. Rep., 6 (2016), https://doi.org/10.1038/srep19087.

[13] M. Neupane, S.-Y. Xu, L. A. Wray, A. Petersen, R. Shankar, N. Alidoust, Chang Liu, A. Fedorov, H. Ji, J. M. Allred, Y. S. Hor, T.-R. Chang, H.-T. Jeng, H. Lin, A. Bansil, R. J. Cava, and M. Z. Hasan, Topological surface states and Dirac point tuning in ternary topological insulators, Phys. Rev. B 85 (2012), https://doi.org/10.1103/PhysRevB.85.235406.

[14] O.E. Tereshchenko, K.A. Kokh, V.V. Atuchin, K.N. Romanyuk, S.V. Makarenko, V.A. Golyashov, A.S. Kozhukhov, I.P. Prosvirin, A.A. Shklyaev, Stability of the (0001) Surface of the Bi_2Se_3 Topological Insulator, JETP Lett. 94 (2011) 465–468, https://doi.org/10.1134/S0021364011180159.

[15] D. Harker. The crystal structure of the mineral tetradymite, Bi_2Te_2S, Z. Kristallogr. 89 (1934) 175-181, https://rruff.info/uploads/ZK89_175.pdf.

[16] A.B. Kuzmenko, Kramers–Kronig constrained variational analysis of optical spectra, Rev. Sci. Instrum. 76 (2005) 083108, https://doi.org/10.1063/1.1979470.

[17] V. Chis, I. Yu. Sklyadneva, K. A. Kokh, V. A. Volodin, O. E. Tereshchenko, and E. V. Chulkov, Vibrations in binary and ternary topological insulators: First-principles calculations

and Raman spectroscopy measurements, Phys. Rev. B 86 (2012), https://doi.org/10.1103/PhysRevB.86.174304.

[18] M.V. Klein, in: M. Cardona (Ed.), Light Scattering in Solids, Springer-Verlag, Berlin, 1975, pp. 147-204, https://doi.org/10.1007/978-3-540-37568-5.

[19] R. Vilaplana, O. Gomis, F. J. Manjón, A. Segura, E. Pérez-González, P. Rodríguez-Hernández, A. Muñoz, J. González, V. Marín-Borrás, V. Muñoz-Sanjosé, C. Drasar, and V. Kucek, High-pressure vibrational and optical study of Bi_2Te_3, Phys. Rev. B 84 (2011), https://doi.org/10.1103/PhysRevB.84.104112.

[20] M. Kanagaraj, Amit Pawbake, Saurav Ch. Sarma, V. Rajaji, Chandrabhas Narayana, Marie-Aude Measson, Sebastian C. Peter, Structural, magnetotransport and Hall coefficient studies in ternary Bi_2Te_2Se, Sb_2Te_2Se and Bi_2Te_2S tetradymite topological insulating compounds**,** J. Alloys Compd, 794 (2019) 195-202, https://doi.org/10.1016/j.jallcom.2019.04.226.

[21] I. V. Zhevstovskikh, Y. S. Ponosov, S. G. Titova, N. S. Averkiev, V. V. Gudkov, M. N. Sarychev, T. V. Kuznetsova, K. A. Kokh, and O. E. Tereshchenko, Anomalous Behavior of the Elastic and Optical Properties in $Bi_{1.5}Sb_{0.5}Te_{1.8}Se_{1.2}$ Topological Insulator Induced by Point Defects, Phys. Status Solidi B, (2018), https://doi.org/10.1002/pssb.201800264.

[22] H.-H. Kung, M. Salehi, I. Boulares, A.F. Kemper, N. Koirala, M. Brahlek, P. Lošťák, C. Uher, R. Merlin, X. Wang, S.-W. Cheong, Seongshik Oh, Girsh Blumberg, Surface vibrational modes of the topological insulator Bi_2Se_3 observed by Raman spectroscopy, Phys. Rev. B 95 (2017), https://doi.org/10.1103/PhysRevB.95.245406.

[23] Yao Tian, Gavin B. Osterhoudt, Shuang Jia, R. J. Cava, and Kenneth S. Burch, Local phonon mode in thermoelectric Bi_2Te_2Se from charge neutral antisites, Appl. Phys. Lett. 108 (2016) 041911, https://doi.org/10.1063/1.4941022.

[24] D. O. Scanlon, P. D. C. King, R. P. Singh, A. de la Torre, S. McKeown Walker, G. Balakrishnan, F. Baumberger, C. R. A. Catlow, Controlling Bulk Conductivity in Topological

Insulators: Key Role of Anti-Site Defects, Adv. Mater. 24 (2012) 2154–2158, https://doi.org/10.1002/adma.201200187.

[25] D. Koumoulis, B. Leung, T. C. Chasapis, R. Taylor, D. King Jr., M.G. Kanatzidis, L.-S. Bouchard, Understanding Bulk Defects in Topological Insulators from Nuclear-Spin Interactions, Adv. Funct. Mater. 24 (2014) 1519–1528, https://doi.org/10.1002/adfm.201302673.

[26] W. Richter, C. R. Becker, A Raman and far-infrared investigation of phonons in the rhombohedral V2–VI3 compounds Bi_2Te_3, Bi_2Se_3, Sb_2Te_3 and $Bi_2(Te_{1-x}Se_x)_3$ ($0 < x < 1$), $(Bi_{1-y}Sb_y)_2Te_3$ ($0 < y < 1$), Phys. Status Solidi B 84 (1977) 619-628, https://doi.org/10.1002/pssb.2220840226.

[27] A. D. LaForge, A. Frenzel, B. C. Pursley, Tao Lin, Xinfei Liu, Jing Shi, and D. N. Basov, Optical characterization of Bi_2Se_3 in a magnetic field: Infrared evidence for magnetoelectric coupling in a topological insulator material, Phys. Rev. B 81 (2010), https://doi.org/10.1103/PhysRevB.81.125120.

[28] N. P. Butch, K. Kirshenbaum, P. Syers, A. B. Sushkov, G. S. Jenkins, H. D. Drew, and J. Paglione, Strong surface scattering in ultrahigh-mobility Bi_2Se_3 topological insulator crystals, Phys. Rev. B 81 (2010) 241301R, https://doi.org/10.1103/PhysRevB.81.241301.

[29] S. V. Dordevic, M. S. Wolf, N. Stojilovic, Hechang Lei and C. Petrovic, Signatures of charge inhomogeneities in the infrared spectra of topological insulators Bi_2Se_3, Bi_2Te_3 and Sb_2Te_3, J. Phys.: Condens. Matter 25 (2013), https://doi.org/10.1088/0953-8984/25/7/075501.

[30] G. Martinez, B. A. Piot, M. Hakl, M. Potemski, Y. S. Hor, A. Materna, S. G. Strzelecka, A. Hruban, O. Caha, J. Novák, A. Dubroka, Č. Drašar & M. Orlita, Determination of the energy band gap of Bi_2Se_3, *Sci Rep*. 7 (2017) 6891, https://doi.org/10.1038/s41598-017-07211-x.

[31] I. Mohelský, A. Dubroka, J. Wyzula, A. Slobodeniuk, G. Martinez, Y. Krupko, B. A. Piot, O. Caha, J. Humlíček, G. Bauer, G. Springholz, and M. Orlita, Landau level spectroscopy of Bi_2Te_3, Phys. Rev. B 102 (2020), https://doi.org/10.1103/PhysRevB.102.085201.

[32] James G. Analytis, Jiun-Haw Chu, Yulin Chen, Felipe Corredor, Ross D. McDonald, Z. X. Shen, and Ian R. Fisher, Bulk Fermi surface coexistence with Dirac surface state in Bi_2Se_3: A comparison of photoemission and Shubnikov–de Haas measurements, Phys. Rev. B 81 (2010), https://doi.org/10.1103/PhysRevB.81.205407.

[33] Bo Zhou, Z. K. Liu, J. G. Analytis, K. Igarashi, S. K. Mo, D. H. Lu, R. G. Moore, I. R. Fisher, T. Sasagawa, Z. X. Shen, Z. Hussain, Y. L. Chen, Controlling the carriers of topological insulators by bulk and surface doping, Semicond. Sci. Technol. 27 (2012), https://doi.org/10.1088/0268-1242/27/12/124002.

Figure captions

Fig. 1. (Color online). XRD patterns of $Bi_{1.1}Sb_{0.9}Te_2S$: (a) experimental data from powder (open circles), Rietveld fit (solid line) and the difference between them as well as a standard set of Bragg reflections corresponding to the tetradymite structure; (b) experimental data from single crystal; (c) CuKα1 and CuKα2 lines for the (0,0,30) and (0,0,33) diffraction peaks for single crystal.

Fig. 2. The Raman susceptibility of $Bi_{1.1}Sb_{0.9}Te_2S$ obtained at two temperatures for the XX and XY geometries (points). Each spectrum was fitted with narrow peaks (dashed lines) and a broad continuum (solid lines). The vertical dashed lines show phonon positions at 10 K.

Fig. 3. An experimental FIR reflectivity spectrum at 4.2 K (symbols) and Drude-Lorentz fit (solid line).

Fig. 4. ARPES energy dispersion relations of $Bi_{1.1}Sb_{0.9}Te_2S$ along the $\bar{\Gamma} - \bar{M}$ direction at 60 K. The inset displays the corresponding Fermi surface map.

Table caption

Table 1. A comparison of center frequencies (cm^{-1}) of Raman and infrared-active phonons for TIs with the $R\bar{3}m$ space group lattice symmetry [17, 26].